Materials Today Energy 27 (2022) 101029

Contents lists available at ScienceDirect

Materials Today Energy

journal homepage: www.journals.elsevier.com/materials-today-energy/

Cubic-spinel $AgIn_5S_8$-based thermoelectric materials: synthesis, phonon transport and defect chemistry

Chaohua Zhang [a, *], Yubo Dou [a], Jiali Chen [a], Susu Fang [b], Weigao Xu [b], Xuelian Wu [a, **], Lipeng Hu [a], Fusheng Liu [a], Yu Li [a], Junqin Li [a, ***]

[a] College of Materials Science and Engineering, Shenzhen Key Laboratory of Special Functional Materials, Shenzhen Engineering Laboratory for Advanced Technology of Ceramics, Guangdong Research Center for Interfacial Engineering of Functional Materials, Institute of Deep Underground Sciences and Green Energy, Shenzhen University, Shenzhen 518060, PR China

[b] Key Laboratory of Mesoscopic Chemistry, School of Chemistry and Chemical Engineering, Nanjing University, Nanjing 210023, PR China

ARTICLE INFO

Article history:
Received 28 March 2022
Received in revised form
26 April 2022
Accepted 27 April 2022
Available online 5 May 2022

Keywords:
Mechanical properties
Defect formation
Density functional theory
$AgIn_5S_8$
Metal sulfides

ABSTRACT

Cubic-spinel $Ag_{1-x}Cu_xIn_5S_8$ is promising as it is a kind of In−S-based thermoelectric material using eco-friendly elements like In, Cu and S. Here, we develop a melting method to synthesize single-phase $Ag_{1-x}Cu_xIn_5S_8$ alloys using metal sulfides as precursors, and we also comprehensively study their thermoelectric properties, chemical bonding, electronic and phonon structures, and defect chemistry. Owing to the complex crystal structures, weak chemical bonding, and "rattling-like" phonon modes, the $Ag_{1-x}Cu_xIn_5S_8$ alloys show low lattice thermal conductivity of ~0.63−0.72 $Wm^{-1}K^{-1}$ at 873 K. The optimal figure of merit (ZT) of the n-type $Ag_{1-x}Cu_xIn_5S_8$ can reach ~0.31 at 873 K, which is higher than the theoretical prediction. The diamond-like crystal structures also enable them to have good mechanical properties, with a hardness of ~3.95 GPa, comparable to those thermoelectric materials with the highest mechanical strength. Our understanding of the "rattling-like" phonon modes and defect chemistry in $AgIn_5S_8$ can also guide the further development of the more promising p-type $AgIn_5S_8$ and other advanced cubic-spinel thermoelectric materials.

1. Introduction

Thermoelectric (TE) materials enable the direct conversion between heat and electricity, showing great promise for sustainable energy applications [1–3]. The performance of a TE material is gauged by a dimensionless figure of merit (ZT) [4]. $ZT = S^2\sigma T/\kappa = S^2\sigma T/(\kappa_{ele}+\kappa_{lat})$, where S, σ, T, κ, κ_{ele} and κ_{lat} are the Seebeck coefficient, electrical conductivity, absolute temperature, total thermal conductivity, electronic and lattice thermal conductivity, respectively. Usually, the S, σ, and κ_{ele} are adversely correlated by the carrier density (n) [4], where the n is required to be optimized for a high power factor (PF, $= S^2\sigma$) and then high ZT. Besides the optimization of n, manipulation of band structures is another important strategy for improving PF [5–7], such as introducing band convergence [7,8] and resonant bands [9]. The κ_{lat} is relatively less coupled with other TE parameters [4], thus lowering κ_{lat} is quite efficient for obtaining a high ZT [2]. To realize low κ_{lat}, strategies of introducing multiscale microstructures [10] and exploring intrinsic low-κ_{lat} TE materials [11,12] are usually proposed.

In addition to developing various strategies for enhancing the ZT of the current TE materials (typically like Bi_2Te_3 [13], PbTe [14], GeTe [15] and $CoSb_3$ [16]), exploring new high-ZT TE materials with advantages of high mechanical strength, high thermal stability, earth-abundance and eco-friendliness is also a key task for realizing the civil applications of TE technology [17]. Recently, numerous efforts focused on those new TE materials with intrinsic low κ_{lat} [11,18–20], which usually had complex crystal structures, weak chemical bonding, lone-pair electrons and rattling atoms. Guided by the well-known concept of "phonon glass and electron crystal" [2,21], many sulfide-like TE materials (such as enargite Cu_3PS_4 [18], argyrodite Ag_9GaS_6 [12] and Ag_8SnS_6 [11], copper chalcogenide Cu_3SbSe_4 [22,23] and $Cu_7Sn_3S_{10}$ [24]) with complex crystal structures and earth-abundant eco-friendly elements attracted great attention, even though their experimental ZTs were still lower than 1.

The cubic-spinel materials generally display the formula of AB_2X_4 with space group symmetry $Fd\bar{3}m$ [25], where the A and B refer to the cations on the tetrahedral sites and octahedral sites,

* Corresponding author.
** Corresponding author.
*** Corresponding author.
E-mail addresses: zhangch@szu.edu.cn (C. Zhang), xuelian.wu@szu.edu.cn (X. Wu), junqinli@szu.edu.cn (J. Li).

https://doi.org/10.1016/j.mtener.2022.101029
2468-6069/

respectively, and X refers to the anions. Typical spinel materials like MFe_2O_4 (M = Mn, Co, Ni) [26], $MgAl_2O_4$ [27] and Si_3N_4 [28] have been extensively studied in various fields owing to their remarkable magnetic, optical, catalytic, electrical and mechanical properties. The cubic-spinel chalcogenide compounds (such as $ZnCr_2Se_4$ [25], $ZnIn_2S_4$ [29], $CdCr_2Se_4$ [30] and $CuTi_2S_4$ [31]) were studied as they are good TE-material candidates for the following reasons. First, the spinel chalcogenides usually possess big primitive cells with short-range disordered elements [25], which could behave as "phonon glass" for low κ_{lat}. Second, the cubic structures generally facilitate multi-valley bands for high *PF*. Third, the diamond-like framework in the cubic-spinel materials should also have good mechanical properties and thermal stability. However, previous experimental trials on these cubic-spinel TE materials indicated poor *ZT*, showing maximum *ZT* in the order of 0.1 [25]. On the contrary, density-functional-theory (DFT) calculations predicted higher *ZT* in some cubic-spinel materials, such as AB_2S_4 (A = Cd and Zn, B= Sc and Y) [32], MgX_2O_4 (X = Rh and Bi) [33], $MgIn_2X_4$ (X = S and Se) [34]. To fill the gap between these experimental results and theoretical predictions, careful studies on material synthesis and defect chemistry are greatly needed.

Recently, a theoretical study has predicted superior TE performance in one kind of cubic-spinel material of $AgIn_5S_8$ ($CuIn_5S_8$) [35], which is expected to have a *ZT* of ~2.22 at 1000 K for p-type $AgIn_5S_8$ while a *ZT* of ~0.2 at 1000 K for n-type $AgIn_5S_8$, showing anisotropic *ZT*. As shown in Fig. 1a, in the supercell crystal structures of $Ag_4In_{20}S_{32}$ and $Cu_4In_{20}S_{32}$, 4 Ag/Cu and 4 In atoms occupy the tetrahedral coordination sites, and the remaining 16 In atoms occupy the octahedral coordination sites, where the $(Ag/Cu\ or\ In)S_4$ tetrahedron and $[In]S_6$ octahedron are connected by sharing edges and corners. The $AgIn_5Se_8$ and $AgIn_5Te_8$ compounds also show similar diamond-like crystal structures but show different space group symmetry $P\bar{4}2m$, only having a tetrahedral connection, which have also been experimentally [36,37] and theoretically [38] studied as new TE materials recently.

In this study, we experimentally realized the synthesis of cubic-spinel $Ag_{1-x}Cu_xIn_5S_8$ alloys by a traditional melting method using metal sulfides (Ag_2S, Cu_2S, In_2S_3) as precursors. We also systemically studied the chemical bonding, electronic/phonon structures, and defect chemistry of $AgIn_5S_8$-based alloys by DFT calculations. The diamond-like network formed by In−S bonding makes the $AgIn_5S_8$ to have a high mechanical performance with a hardness of ~3.95 GPa, while the weak bonding of Ag/Cu−S and "rattling-like" Ag/Cu atoms make the $Ag_{1-x}Cu_xIn_5S_8$ alloys to have a low κ_{lat} of ~0.63−0.72 $Wm^{-1}K^{-1}$ at 873 K. Owing to the lower formation energy of the intrinsic defects of $In_{Ag}^{\bullet\bullet}$, the as-prepared $AgIn_5S_8$ exhibit intrinsic n-type semiconducting behaviors. This understanding of defect mechanisms in $AgIn_5S_8$ provides a guide for the realization of the more promising p-type $AgIn_5S_8$ and other cubic-spinel TE materials.

2. Experimental section

2.1. Samples preparation

Raw materials of Ag_2S, In_2S_3 and Cu_2S with 99.99% purity were used to synthesize $Ag_{1-x}Cu_xIn_5S_8$. After weighing, the raw materials were sealed in quartz tubes, then heated to 1100 °C in 5 h and kept at this temperature for 5 h. After the reaction, the products were slowly cooled down to 850 °C in 80 min and held at 850 °C for 24 h. Then the as-prepared ingots were cooled down to room temperature and grounded to powders with an agate mortar and pestle. The powders were sintered at 700 °C for 10 min by the spark plasma sintering (SPS) system in a Φ20 mm graphite die under a pressure of 60 MPa. The bulk pellets were then cut into 4 mm×4 mm×12 mm and 10 mm×10 mm×2 mm for the characterizations of electrical and thermal properties, respectively.

2.2. Characterization methods

Powder X-ray diffraction (XRD, Bruker D8-Advance) was performed for structural characterizations using Cu Kα radiation (40 kV × 200 mA). Raman spectra were acquired using a micro-Raman spectrometer (Horiba-LabRAM HR) with a × 50 objective lens (numerical aperture = 0.5). The 600 lines per mm gratings were used in the Raman measurements and the excitation energy was set as 2.33 eV. The morphology and elemental analysis were characterized by scanning electron microscopy (SEM, Hitachi SU-70) equipped with energy dispersive spectroscopy (EDS). Electrical properties (*S* and σ) were measured using a ZEM-2 instrument (Ulvac-Riko) in a helium atmosphere. The thermal conductivity κ ($\kappa = \lambda d C_p$) was determined by measuring the thermal diffusivity (λ) using the laser flash method (LFA-467, NETZSCH), the density (d) using the Archimedes method and the specific heat capacity (C_p) using the Dulong-Petit law. The Hall carrier density was measured by the commercial physical properties measurement systems (PPMS, Quantum Design). The uncertainty of σ, *S* and κ was estimated to be around ±3%, ±5% and ±5% respectively, and then the uncertainty of *PF* and *ZT* was calculated to be ±13% and ±18%, respectively. The error bars in most figures were not displayed to keep good readability.

2.3. Theoretical calculations

To calculate the electron and phonon structures of $AgIn_5S_8$ ($CuIn_5S_8$) and the corresponding defect formation energy, the Vienna Ab initio Simulation Package (VASP) was used for the DFT calculations [39], using the cubic supercell models of $Ag_4In_{20}S_{32}$. The Perdew-Burke-Ernzerh of exchange-correlation function (GGA-PBE) and projector enhanced wave (PAW) type pseudopotentials were used [40,41]. The cut-off energy of the plane-wave basis was set to be 450 eV, and the energy convergence criterion was set as 10^{-6} eV/cell. A dense k-mesh of 5×5×5 sampling with the Monkhorse-Pack mode was used [42]. The spin-orbit coupling effects were also taken into account in determining the band structures, and density of states. The crystal structure, electron localization function (ELF) images, and charge density were visualized using the VESTA software [43]. A finite-displacement method was used for calculating the phonon structures of $AgIn_5S_8$. After structural relaxation of $AgIn_5S_8$, supercells of 2×2×2 with atomic displacements were constructed by the Phonopy code [44]. After calculation by the VASP code, the Phonopy code was used to determine the forces sets and then the phonon dispersion and density of states.

3. Results and discussion

3.1. Chemical bonding and electronic structures

To understand the chemical bonding and electronic structures of $AgIn_5S_8$-based alloys, DFT calculations were performed based on the supercell model of $(Ag/Cu)_4In_{20}S_{32}$ (Fig. 1a). Fig. 1b shows the ELF images of $AgIn_5S_8$ in the (110) and (111) planes. The ELF provides a useful tool to identify the atomic shell structure, bonding and lone-pair electrons [45]. The ELF values are limited to the range of 0−1, where the upper limit ELF = 1 represents perfect electron localization, ELF = 0.5 represents the electron-gas-like pair probability for bonding and ELF = 0 represents perfect electron delocalization [45]. The ELF values between In and S is much higher

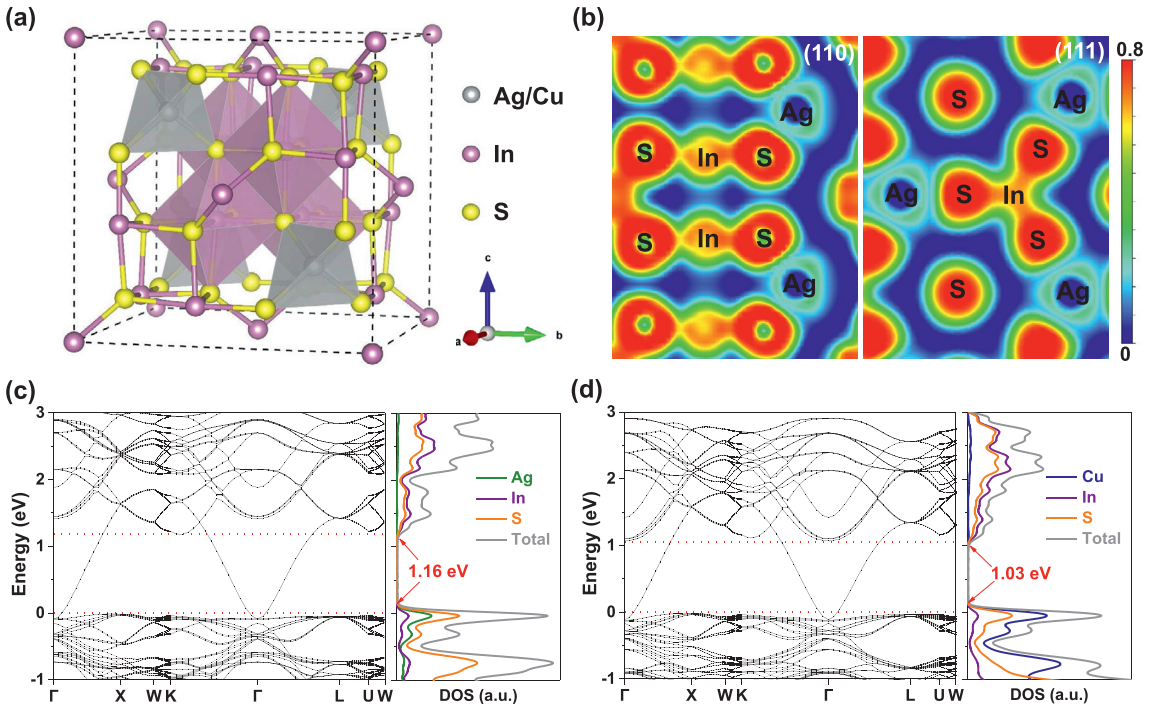

Fig. 1. DFT calculations. (a) The cubic crystal structure of $AgIn_5S_8$ or $CuIn_5S_8$. (b) Electron-localization-function (ELF) images of $AgIn_5S_8$ in the (110) plane and (111) plane. Band structures and corresponding density of states (DOS) of (c) $AgIn_5S_8$ and (d) $CuIn_5S_8$ using the supercell of $Ag_4In_{20}S_{32}$ and $Cu_4In_{20}S_{32}$, respectively.

than that between Ag and S, demonstrating stronger bonding between In and S but weaker bonding between Ag and S, and the underlying reason may be due to higher electronegativity difference of In—S compared to that of Ag—S. The weak bonding of Ag may facilitate the "rattling-like" behaviors for enhancing the TE properties of $AgIn_5S_8$-based alloys, as discussed below.

Owing to the same crystal structures, the band structures of $AgIn_5S_8$ and $CuIn_5S_8$ are almost the same (Fig. 1c—d), and the slight difference between the two should be ascribed to the weaker bonding of Cu—S than Ag—S (Fig. S1). Interestingly, the band structures shown in Fig. 1c—d seem to indicate the metallic behavior of $AgIn_5S_8$ and $CuIn_5S_8$, but the density of states (DOS) between the energy region highlighted by dash lines are almost negligible. The bands with quite small DOS are mainly from the contribution of In and S orbitals (Fig. S2). By neglecting the quite small DOS between the dash lines, the calculated gap between the dash lines for $AgIn_5S_8$ and $CuIn_5S_8$ are about 1.16 eV and 1.03 eV, respectively, which seem to agree with the experimental optical band gap [46]. The delocalized parabolic bands with negligible DOS, as revealed by DFT calculations, may contribute very limited conducting channels for the electron transport, as experimentally shown below. The S and In orbitals both show contributions to the valence bands (VBs) and conduction bands (CBs), while the Ag/Cu orbitals nearly only show the contribution to the VBs. Owing to the more delocalized electrons around Cu than Ag (Fig. S1), the contribution of Cu to the VBs is much stronger than that of Ag. The CBs mostly show parabolic dispersion with low DOS, but the VBs display the combination of flat and dispersive bands with high DOS. The combination of heavy and light bands in VBs may alleviate the disadvantage of single heavy bands for low carrier mobility [35]. Therefore, $AgIn_5S_8$ and $CuIn_5S_8$ should have a high *PF* in p-type but a lower *PF* in n-type, as demonstrated by the Boltzmann transport calculations from R. Juneja et al. [35].

3.2. Synthesis of $AgIn_5S_8$-based alloys using metal sulfides as precursors

Considering the interesting electronic structure of $AgIn_5S_8$ for TE applications, we employed the pseudo-binary phase diagram of Ag_2S—In_2S_3 [47] (Fig. S3) for designing the synthesis process of $AgIn_5S_8$. The synthesis condition was set as follows: melting at 1100 °C for reaction and then thermal annealing at 850 °C for ensuring good stoichiometry. We tried to use the traditional elemental melting method to synthesize $AgIn_5S_8$ using the precursors of Ag, In and S, but the loaded quartz tubes can be easily burst during the melting process owing to the high saturated vapor pressure of S. High-frequency smelting could be used to successfully obtain ingot samples using the precursors of Ag, In and S, but the as-prepared samples usually have many mixed phases (possibly like In_6S_7 and $AgInS_2$), as indicated in the XRD data (Fig. S3). Alternatively, by using metal sulfides of Ag_2S and In_2S_3 as the precursors, we could easily employ the traditional melting method to obtain single-phase $AgIn_5S_8$, whose XRD pattern was well-matched with the standard pattern (PDF # 25—1329) without secondary phases (Fig. S3).

Using the above method, we successfully prepared the $Ag_{1-x}Cu_xIn_5S_8$ alloys by further replacing the precursor Ag_2S with Cu_2S, as confirmed by the corresponding XRD patterns shown in Fig. 2a. The Rietveld-refinement derived lattice parameter (*a*) decreases linearly with the composition x, following the Vegard's law, which indicates the single solid solution of $Ag_{1-x}Cu_xIn_5S_8$ (Fig. 2b). The complete miscibility between $AgIn_5S_8$ and $CuIn_5S_8$ is mainly ascribed to the same crystal structures and little difference in *a*. The shrinkage of *a* with the increase of *x* in $Ag_{1-x}Cu_xIn_5S_8$ is ascribed to the smaller ion radius of Cu than that of Ag. The SEM and EDS elemental mapping images show homogeneous microstructures and uniform distribution of each element (Fig. 2c—d), further

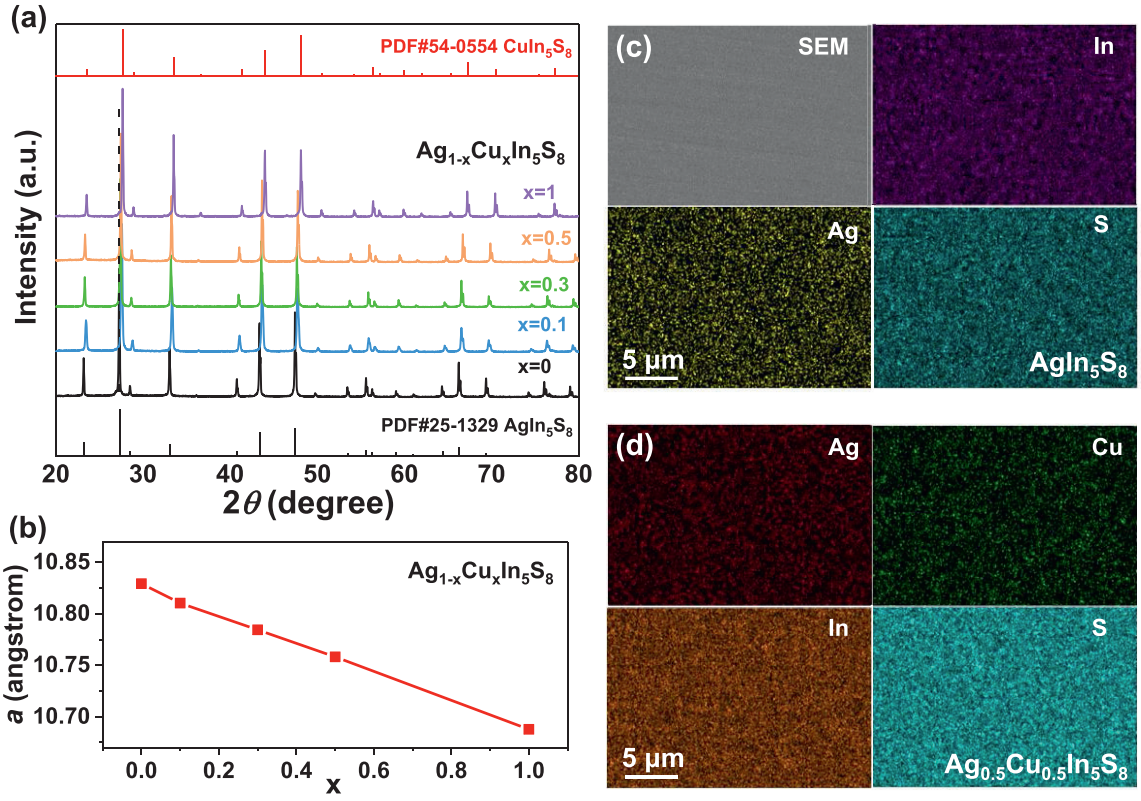

Fig. 2. Synthesis of $Ag_{1-x}Cu_xIn_5S_8$. (a) XRD patterns of $Ag_{1-x}Cu_xIn_5S_8$. (b) Composition-dependent lattice parameter *a* derived from the Rietveld refinement of the XRD patterns in (a). SEM and elemental mapping images of the representative (c) $AgIn_5S_8$ and (d) $Ag_{0.5}Cu_{0.5}In_5S_8$.

demonstrating the single phases of $Ag_{1-x}Cu_xIn_5S_8$ without secondary phases, which is consistent with the XRD results (Fig. 2a–b).

3.3. Thermoelectric properties of $Ag_{1-x}Cu_xIn_5S_8$

Fig. 3 and Table 1 display the TE properties of $Ag_{1-x}Cu_xIn_5S_8$. All the $Ag_{1-x}Cu_xIn_5S_8$ alloys show negative *S*, demonstrating n-type conducting behavior (Fig. 3a). With the increase of Cu content *x*, the *S* shows an increasing tendency while the σ displays a decreasing tendency (Fig. 3a), which is mainly ascribed to the decrease of *n* (Fig. 3c). The *n* of $Ag_{1-x}Cu_xIn_5S_8$ decreases from ~1.06×10^{19} cm^{-3} for the $x = 0$ sample to ~0.55×10^{19} cm^{-3} for the $x = 1$ sample. As Ag and Cu are the same-group elements, the slight change of *n* by increasing Cu content *x* should be mainly ascribed to the change of chemical bonding, which may affect the formation energy of some intrinsic defects. On the other hand, the decrease of lattice parameters (Fig. 2b) and evolution of band structures (Fig. 1d) by Cu alloying may also affect the Fermi level of $Ag_{1-x}Cu_xIn_5S_8$ for tuning the *n*. Noted that the σ does not monotonically decrease with temperature like traditional heavily-doped TE materials. Instead, the σ displays an increasing tendency with temperature, suggesting the semiconducting behavior with temperature-dependent *n*. Owing to the relatively higher *n* in $x = 0$ and $x = 0.1$ samples, the corresponding σ shows a decreasing tendency above 600 K, showing metallic conducting behavior at high temperatures. Besides *n*, the carrier mobility μ is the other factor influencing the σ. We calculated the weight mobility (μ_W) with an empirical equation [48], using the experimental data of σ and *S*. As revealed by the temperature-dependent μ_W (Fig. S4), the carrier scattering mechanism should be dominated by the acoustic phonon scatterings at higher temperatures (>500 K), though carrier scatterings from ionized impurities or grain boundaries may show up in some samples near room temperature.

As shown in Fig. 3b, the κ_{lat} is estimated by subtracting the κ_e from κ as follows,

$$\kappa_{lat} = \kappa - \kappa_e = \kappa - L\sigma T \quad (1)$$

where the Lorenz number *L* is calculated based on a single-parabolic-band approximation [49]. The κ and κ_{lat} of $Ag_{1-x}Cu_xIn_5S_8$ both decrease with the increase in temperature (Fig. 3b), which is ascribed to the dominated *Umklapp* phonon-phonon scattering process at higher temperatures. The κ_{lat} is ~2.12 $Wm^{-1}K^{-1}$ at 300 K and ~0.72 $Wm^{-1}K^{-1}$ at 873 K for $AgIn_5S_8$, and ~1.79 $Wm^{-1}K^{-1}$ at 300 K and ~0.66 $Wm^{-1}K^{-1}$ at 873 K for $CuIn_5S_8$. Owing to the alloying effect, the κ_{lat} of $Ag_{1-x}Cu_xIn_5S_8$ at 300 K firstly decreases ($x = 0$ to $x = 0.5$) then increases ($x = 0.5$ to $x = 1$) with Cu content *x*, resulting in the lowest κ_{lat} of ~1.53 $Wm^{-1}K^{-1}$ at 300 K and ~0.63 $Wm^{-1}K^{-1}$ at 873 K for the $x = 0.5$ sample.

As shown in Fig. 3d, the *PF* of $Ag_{1-x}Cu_xIn_5S_8$ can be optimized by Cu alloying owing to the optimization of *n* (Fig. 3c). The maximized *PF* can reach ~378 $\mu Wm^{-1}K^{-2}$ at 723 K for $Ag_{0.5}Cu_{0.5}In_5S_8$, which is ~32% higher than that of $AgIn_5S_8$. The low *PF* should be mainly ascribed to the quite small DOS effective mass m^*~0.2 m_e (Fig. 3c), where the m_e is mass of free electron. The experimentally fitted small m^* agrees with the calculated band structures of $AgIn_5S_8$ and $CuIn_5S_8$, whose CBs have much smaller DOS than that of VBs (Fig. 1c–d). The low *PF* of n-type $Ag_{1-x}Cu_xIn_5S_8$ makes the corresponding *ZT* not very high even though the κ_{lat} is small. The optimized *ZT* of n-type $Ag_{1-x}Cu_xIn_5S_8$ can reach to ~0.31 at 873 K for the $x = 0.5$ sample.

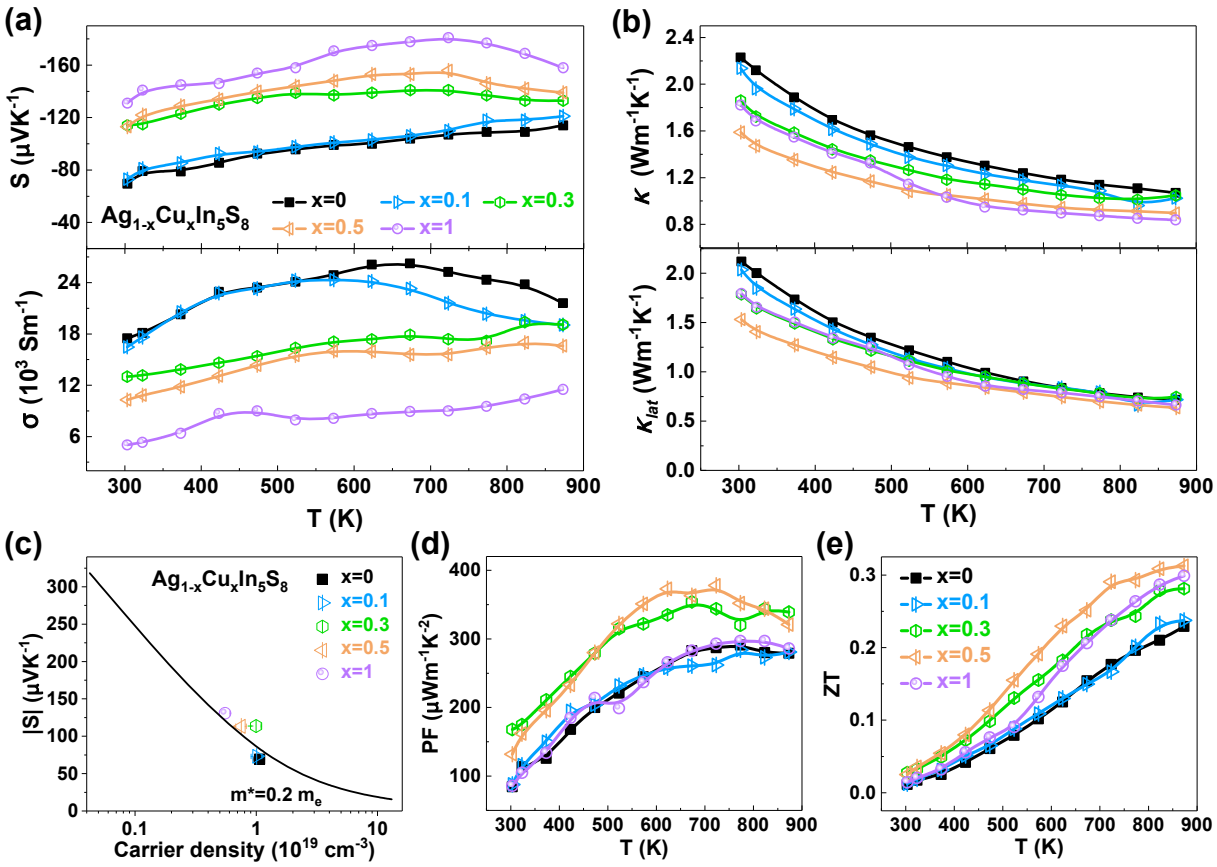

Fig. 3. Thermoelectric properties of $Ag_{1-x}Cu_xIn_5S_8$. Temperature-dependent (a) *S* and σ, (b) κ and κ_{lat} of $Ag_{1-x}Cu_xIn_5S_8$. (c) Carrier-density-dependent *S* at 300 K for $Ag_{1-x}Cu_xIn_5S_8$. Temperature-dependent (d) *PF* and (e) *ZT* of $Ag_{1-x}Cu_xIn_5S_8$. The solid line in (c) is calculated based on the single parabolic band model with a density-of-state effective mass m^* set as 0.2 m_e.

Table 1
Thermoelectric properties of $Ag_{1-x}Cu_xIn_5S_8$ at 300 K.

x	*S* (μVK^{-1})	σ (10^3 Sm^{-1})	*PF* ($\mu Wm^{-1}K^{-2}$)	κ ($Wm^{-1}K^{-1}$)	κ_{lat} ($Wm^{-1}K^{-1}$)	*n* (10^{19} cm^{-3})
0	−69.5	17.5	84.4	2.23	2.12	1.06
0.1	−73.0	16.5	87.9	2.14	2.03	1.01
0.3	−114	13.0	168	1.86	1.79	1.00
0.5	−113	10.3	132	1.59	1.53	0.75
1	−131	5.03	85.9	1.82	1.79	0.55

3.4. Mechanical properties of $Ag_{1-x}Cu_xIn_5S_8$

Besides the TE performance, mechanical performance is also a key factor for a good TE material. For example, $CoSb_3$ skutterudite [7,50] and half-Heusler alloys [51] have attracted great attention recently due to their outstanding mechanical properties and thermal stability, even though their *ZTs* are much lower than other traditional VI-VI compounds like PbTe [52] and GeTe [15]. As shown in Fig. 4a, the nano-indentation test on $Ag_{1-x}Cu_xIn_5S_8$ samples is performed to determine their mechanical properties. The derived Young's modulus of $Ag_{1-x}Cu_xIn_5S_8$ is around 71.3−79.3 GPa and the derived hardness is about 3.67−3.95 GPa. As shown in Fig. 4b, the hardness of $AgIn_5S_8$ is much higher than that of Mg_3Sb_2 [53], GeTe [54], Bi_2Te_3 [55] and PbTe [56], and is at the same level as the TE materials of $CoSb_3$ [57] and MgAgSb [58] that show superior mechanical performance. The intrinsic high mechanical performance of $AgIn_5S_8$ should be mainly ascribed to the strong In−S chemical bonding for forming the main diamond-like framework.

3.5. Phonon structures and thermal transport

The mechanism of intrinsic low κ_{lat} in $AgIn_5S_8$ has been theoretically argued by a "rattling" phonon mode [35], As shown in Fig. 5, we further perform the phonon dispersion, Raman spectroscopy, and heat capacity measurements to understand the mechanism of "rattling-like" phonon modes in $AgIn_5S_8$. The phonon dispersion of $AgIn_5S_8$ shows no imaginary frequencies (Fig. 5a), demonstrating its dynamical stability. The phonon DOS indicates that heavy atoms of In and Ag mostly contribute to the acoustic and optical phonon branches in the low-frequency range (<5 THz), whereas the lighter S atoms dominate the high-frequency optical phonon branches above 5 THz. As highlighted in the DOS, most of the Ag contribution lies in the low-frequency optical phonons around 2 THz, which should be ascribed to the weaker bonding between Ag and S, forming "rattling-like" optical phonons. The "rattling" behavior generally increases the lattice anharmonicity and flattens the phonon dispersion [59], which is usually considered as an effective way to reduce the κ_{lat}. In principle, the

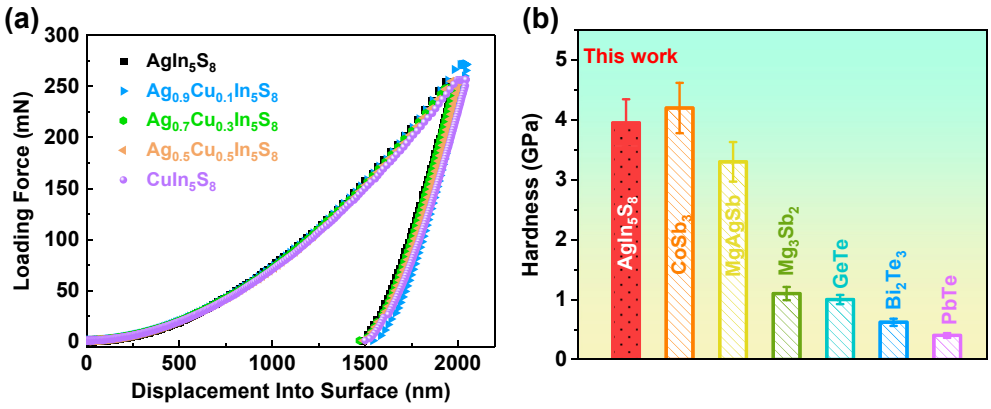

Fig. 4. Mechanical properties of $Ag_{1-x}Cu_xIn_5S_8$. (a) Plots of loading force vs. indentation depth for the nano-indentation test of $Ag_{1-x}Cu_xIn_5S_8$. (b) The hardness of our $AgIn_5S_8$ in comparison with other typical TE materials including $CoSb_3$ [57], MgAgSb [58], Mg_3Sb_2 [53], GeTe [54], Bi_2Te_3 [55] and PbTe [56].

κ_{lat} is dominated by the acoustic phonon branches [60], and therefore small contribution of acoustic phonons to total phonons of $AgIn_5S_8$ is beneficial for a low κ_{lat}.

As shown in Fig. 5b, Raman spectrum is used to experimentally demonstrate the DFT calculated optical phonons of $AgIn_5S_8$. The much obvious Raman peaks at ~48 cm^{-1},66 cm^{-1}, ~180 cm^{-1} and ~326 cm^{-1} agree well with the theoretical optical phonons at ~1.44 THz, ~1.98 THz, ~5.41 THz and ~9.78 THz, respectively, as marked in Fig. 5a. Other weaker peaks marked in Fig. 5b are related to the corresponding optical phonons at G sites of the phonon dispersion in Fig. 5a. To understand the thermal transport, the low-temperature heat capacity (C_P) of $AgIn_5S_8$ is also measured from 2 to 250 K (Fig. 5c). The Debye and Einstein models are usually used to fit the C_P [11,24], as shown in the following equations,

$$C_P^{Debye}(T/\theta_D) = 9R\left(\frac{T}{\theta_D}\right)^3 \int_0^{\theta_D/T} \frac{x^4 e^x}{(e^x-1)^2} dx \quad (2)$$

$$C_P^{Einstein}(T/\theta_E) = 3R\left(\frac{\theta_E}{T}\right)^2 \frac{e^{\theta_E/T}}{(e^{\theta_E/T}-1)^2} \quad (3)$$

where the R is the universal gas constant (~8.31 J $mol^{-1}K^{-1}$), θ_D is the Debye temperature and θ_E is the Einstein temperature. At higher temperatures, the C_P calculated by the Debye and Einstein models both tend to be the classic Dulong-Petit limit of 3 k_B/atom (k_B is the Boltzmann constant). Although the Debye and Einstein models can fit well the C_P in a lower temperature (<30 K) and a higher temperature (>120 K), respectively, neither of them can fit well the C_P in the whole temperature range. Generally, the Debye and Einstein models work well for the acoustic phonons and optical phonons, respectively. Therefore, we used a simple mixed model (1 Debye+2Eienstein) to fit the experimental C_P, as shown in the following equations,

$$C_P = x_D C_P^{Debye}(T/\theta_D) + x_{E1} C_P^{Einstein}(T/\theta_{E1}) + x_{E2} C_P^{Einstein}(T/\theta_{E2}) \quad (4)$$

$$x_D + x_{E1} + x_{E2} = 1 \quad (5)$$

where the x_D is the fraction of the Debye model with a cut-off frequency of $k_B\theta_D/h$ (h is the Planck constant), the x_{E1} and x_{E2} are 2 E models using two representative optical phonons in a low frequency of $k_B\theta_{E1}/h$ and a high frequency of $k_B\theta_{E2}/h$, respectively. The fitted θ_D, θ_{E1} and θ_{E2} are 145 K (3.01 THz), 96 K (2.00 THz) and 335 K (6.98 THz), and the fitted x_D, x_{E1} and x_{E2} are 9%, 25% and 66% respectively. The "low-lying" optical phonon mode around 2 THz (Fig. 5a–b) is also reflected by this theoretical fitting of C_P. The small contribution of the Debye model further proves the small contribution of acoustic phonons for thermal transport in $AgIn_5S_8$, leading to a low κ_{lat}.

Therefore, the phonon dispersion, Raman test and analysis of heat capacity demonstrate the existence of the "rattling" mode in $AgIn_5S_8$, which can increase the lattice anharmonicity for a low κ_{lat}. As shown in Fig. 5d, a Debye-Callaway model [61] is used to fit the κ_{lat} of $AgIn_5S_8$. When only considering the acoustic phonon-phonon scattering process and using the measured phonon velocity (Supporting Information, Table S1), the Grüneisen parameter γ representing the lattice anharmonicity is fitted to be ~2.4, which is higher than many other traditional TE materials with an intrinsic low κ_{lat} [59]. The intrinsic high γ in $AgIn_5S_8$ should be mainly ascribed to the weak chemical bonding of Ag–S and the rattler-like Ag atoms. The theoretical limit of κ_{lat} of $AgIn_5S_8$ is estimated to be ~0.6 $Wm^{-1}K^{-1}$ within 300–873 K, which is close to the experimental value of ~0.72 $Wm^{-1}K^{-1}$ at 873 K for $AgIn_5S_8$.

3.6. Defect formation energy and defect analysis of $AgIn_5S_8$

For n-type $AgIn_5S_8$, our experimental ZT (Fig. 3e) agrees well with the theoretical ZT calculated by R. Juneja et al. [35], which drives us to further develop the more promising p-type $AgIn_5S_8$ that shows theoretical ZT above 2. However, all of our $AgIn_5S_8$-based alloys show n-type behavior, even though we have performed many other experimental trials, such as adding extra In (Fig. S5), In_2S_3 (Fig. S6) and Ag (Fig. S7) during the synthesis process of $AgIn_5S_8$. The Mg_3Sb_2-based TE alloys only showed p-type conducting behavior with poor ZT for a long time but turned out to be good n-type TE materials since 2016 resulting from the good understanding of the Mg defect chemistry in Mg_3Sb_2 [62], which inspired us to understand the defect chemistry of $AgIn_5S_8$.

Fig. 6a and b displays the formation energies of those typical intrinsic defects in $AgIn_5S_8$ under S-poor and S-rich conditions, respectively, such as the S vacancy (V_S), Ag vacancy (V_{Ag}), In vacancy at tetrahedral coordination sites ($V_{In(1)}$) and at the octahedral coordination sites ($V_{In(2)}$) and the antisite defects between the Ag and In at the tetrahedral coordination sites (Ag_{In}, In_{Ag}). The calculation details can be found in the supporting information and Tables S2–S3, and the defect formation equations are listed as follows:

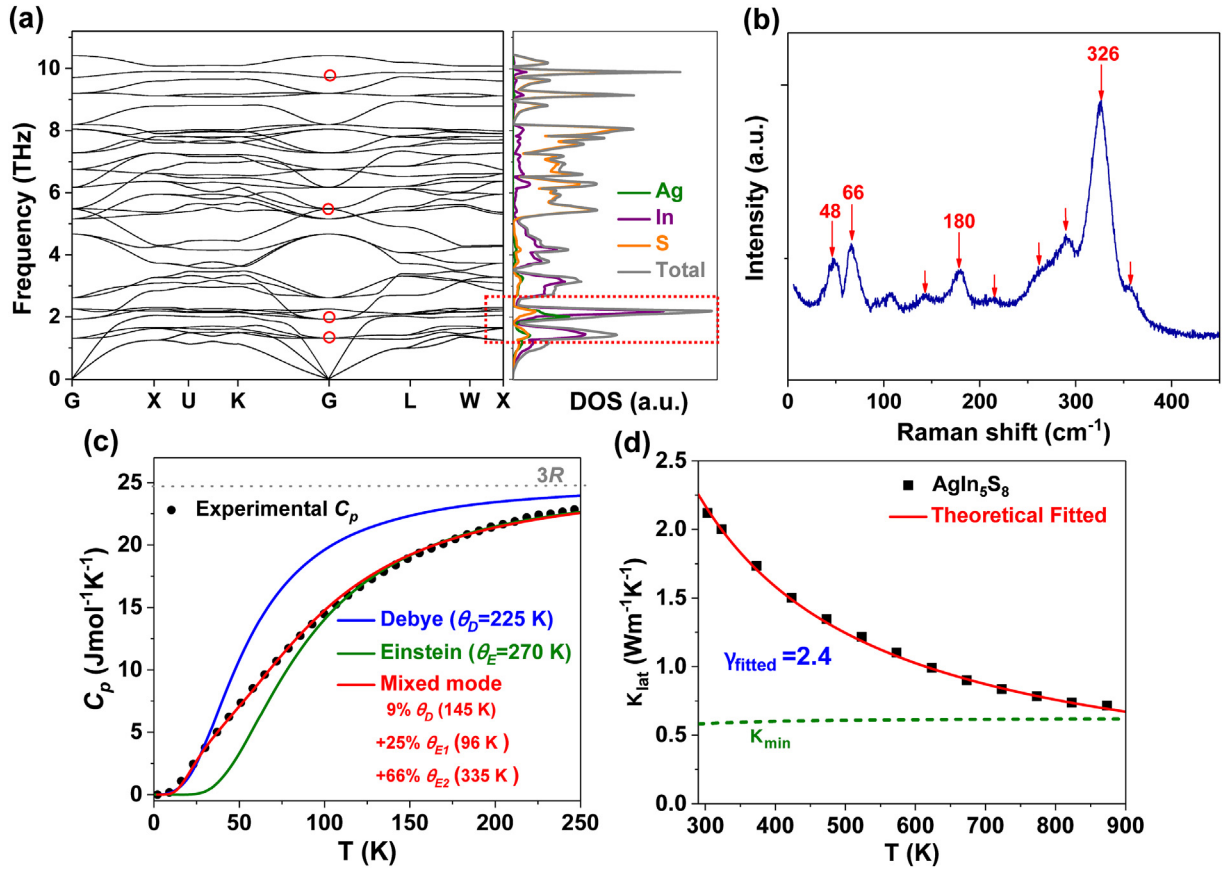

Fig. 5. Phonon transport analysis of $AgIn_5S_8$. (a) Phonon dispersion and corresponding density of states (DOS) of $AgIn_5S_8$. (b) Raman spectrum of $AgIn_5S_8$. (c) The temperature-dependent heat capacity of $AgIn_5S_8$, which is fitted by the Debye model, Einstein model and corresponding mixed model. (d) Theoretical fitting of the κ_{lat} of $AgIn_5S_8$ by a traditional Debye-Callaway model. The red-open-circle marks in (a) correspond to the phonon energy at G point, consistent with the energy measured by Raman in (b).

$$S_S \rightarrow V_S^{\bullet\bullet} + S(g) + 2e' \quad (6)$$

$$Ag_{Ag} \rightarrow V'_{Ag} + Ag(s) + h^{\bullet} \quad (7)$$

$$In_{In} \rightarrow V'''_{In} + In(s) + 3h^{\bullet} \quad (8)$$

$$In_{In} + Ag \rightarrow Ag''_{In} + In(s) + 2h^{\bullet} \quad (9)$$

$$Ag_{Ag} + In \rightarrow In^{\bullet\bullet}_{Ag} + Ag(s) + 2e' \quad (10)$$

Eqs. (6) and (10) represent the n-type doping case, while Eqs. (7)–(9) represent the p-type doping cases. Owing to the strong chemical bonding between In and S (Fig. 1b), the formation energy $V_{In(2)}$ is much higher than that of $V_{In(1)}$ under both S-rich and S-poor conditions (Fig. 6a–b). Therefore, the antisite defects between the Ag and In are only considered at the tetrahedral coordination sites in our DFT calculations. The much higher formation energy of V'''_{In} than that of other defects indicates that the V'''_{In} is not the main intrinsic defect in $AgIn_5S_8$ (Fig. 6a–b), thus the V'''_{In} defect is not discussed in the following defect analysis.

Under S-poor conditions (Fig. 6a), the defect formation energy of $V_S^{\bullet\bullet}$ (~0.49 eV) and $In^{\bullet\bullet}_{Ag}$ (~-0.22 eV) for n-type behavior are much lower than that of V'_{Ag} (~1.36 eV) and Ag''_{In} (~2.13 eV) for p-type behavior. Therefore, the intrinsic n-type behavior in $AgIn_5S_8$-based alloys can be ascribed to the easily-formed intrinsic defects of $V_S^{\bullet\bullet}$ and $In^{\bullet\bullet}_{Ag}$. We especially calculated the band structure of $Ag_3In_{21}S_{32}$ with an antisite defect of $In^{\bullet\bullet}_{Ag}$, which displayed a similar band structure with $Ag_4In_{20}S_{32}$ but a strong n-type doping behavior (Fig. S8). It is generally favorable to obtain p-type doping when the anion-site element is rich [63]. However, even under S-rich conditions (Fig. 6b), the formation energy of V'_{Ag} (1.26 eV) and Ag''_{In} (0.96 eV) for p-type behavior is still not obviously lower than that of $V_S^{\bullet\bullet}$ (1.41 eV) and $In^{\bullet\bullet}_{Ag}$ (0.95 eV) for n-type behavior, making it very hard to obtain p-type $AgIn_5S_8$. Eqs. (6) and (10) for n-type doping mechanism should happen during the synthesis process, and the pull-out Ag and S may form the Ag_2S, leading to the incomplete reaction for Ag_2S precursor, as shown in Eq. (11) below.

$$S + 2Ag \rightarrow Ag_2S \quad (11)$$

By experimentally adding extra In or In_2S_3 in $AgIn_5S_8$ (Figs. S5–S6), the S shows a small decreasing tendency while the σ displays an increasing tendency, indicating the n-type doping behavior of extra In and In_2S_3, which agrees with the defect formation mechanism in Eq. (10). On the contrary, by adding extra Ag or Ag_2S (Figs. S7 and 6c), the S shows an obvious increasing tendency while the σ displays a decreasing tendency, indicating p-type doping behavior of extra Ag or Ag_2S. As shown in Fig. 6c, by adding Ag_2S content in $AgIn_5S_8(Ag_2S)_x$, the S increases slowly at a lower x ($x<1.8\%$) while it dramatically increases at $x = 1.8\%$. The room-temperature σ of $AgIn_5S_8(Ag_2S)_x$ can dramatically decrease from ~1.75×10^4 Sm^{-1} for $x = 0$ to ~0.36 Sm^{-1} for $x = 1.8\%$, decreasing by nearly four orders of magnitude. The reduction of n by adding Ag or Ag_2S agrees with the defect-formation mechanism in (Eqs. 9–11), wherein the formation of Ag''_{In} is more favorable whereas the formation of $In^{\bullet\bullet}_{Ag}$ is suppressed. Given that Ag_2S can induce S-rich

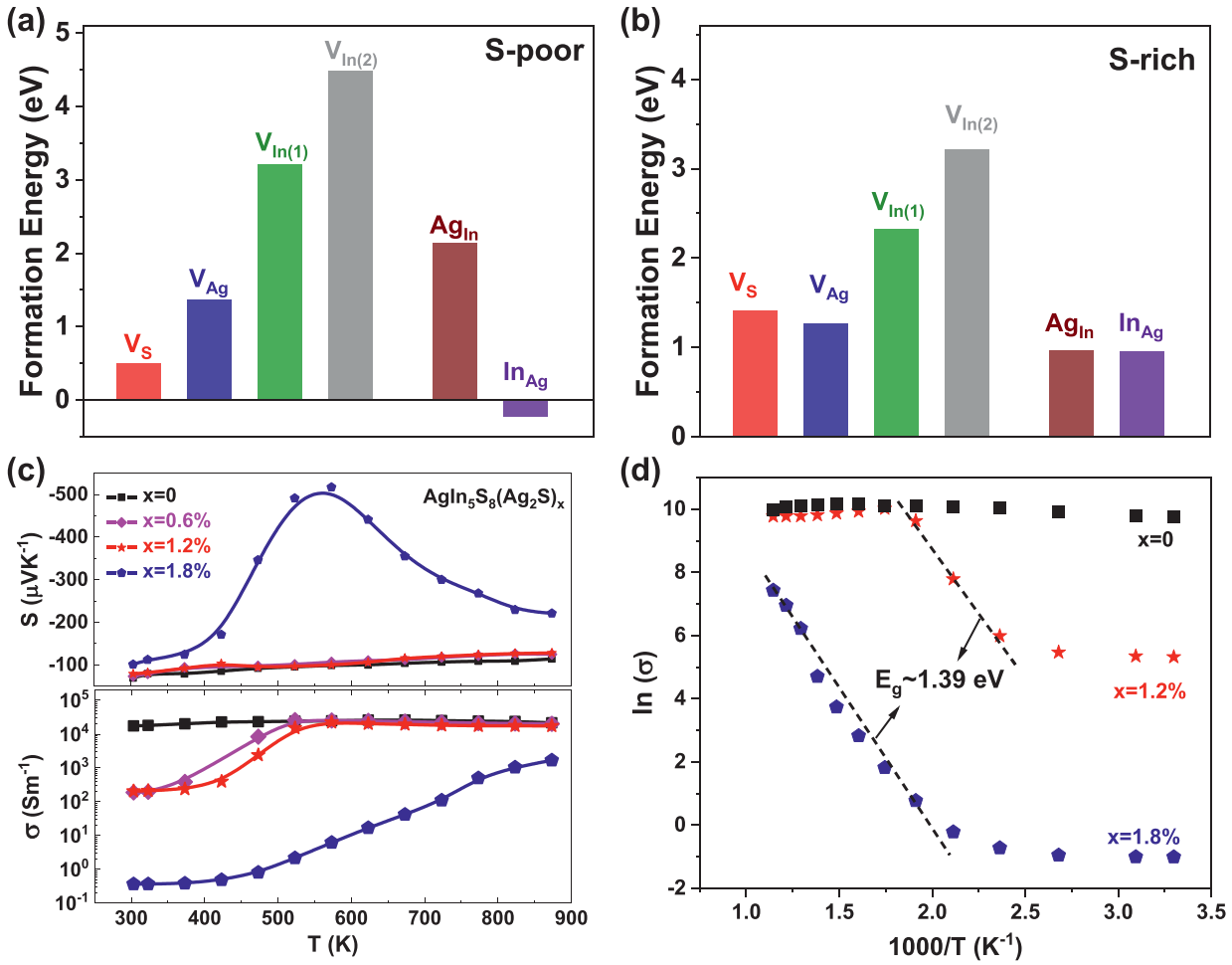

Fig. 6. Defect analysis of $AgIn_5S_8$. The formation energy of different defects based on DFT calculations under the neutral charge condition and (a) S-poor and (b) S-rich conditions. (c) Temperature-dependent of S and σ for $AgIn_5S_8(Ag_2S)_x$. (d) Analysis of the ln(σ)-T^{-1} curve for $AgIn_5S_8(Ag_2S)_x$.

conditions, adding extra Ag_2S is more efficient for introducing p-type doping than adding Ag (Fig. 6c and S7). Further addition of Ag (>3%) and Ag_2S (>1.8%) can even make the σ too low to be detected by our instrument. Although extra Ag_2S is an effective p-type dopant, the addition of Ag_2S still cannot realize the transition from n-type to p-type $AgIn_5S_8$, which should be ascribed to the limited solubility of Ag in $AgIn_5S_8$ (Fig. S9) as well as a higher formation energy of Ag''_{In} than that of $In^{\bullet\bullet\bullet}_{Ag}$ even under S-rich conditions (Fig. 6b). The reduction of n by adding extra Ag_2S do not improve the TE performance of $AgIn_5S_8$, which should be ascribed to the small effective mass (Fig. 3c), originating from the small DOS in conduction bands (Fig. 1c).

For intrinsic semiconductors under acoustic phonon scattering, the σ generally shows to be dependent on the bandgap (E_g) [64].

$$\sigma \propto \exp\left(-\frac{E_g}{2k_BT}\right) \tag{12}$$

As shown in Fig. 6d, the ln(σ) vs. T^{-1} curve is plotted to understand the electrical conducting mechanisms and the E_g of $AgIn_5S_8$ is calculated to be ~1.39 eV, which is quite close to the experimental optical band gap [46]. Owing to the suppression of intrinsic n-type defects by adding extra Ag_2S from $x = 0$–1.8%, the Fermi level (E_F) is lowered toward the VBs and the intrinsic semiconducting property becomes the dominant conducting mechanism, especially for the $x = 1.8\%$ sample. For the $x = 1.8\%$ sample, the S dramatically increases from ~100 μVK^{-1} at 300 K to a peak of ~517 μVK^{-1} at 573 K while it then decreases to ~220 μVK^{-1} at 873 K (Fig. 6c), indicating the dominant bipolar transport at higher temperatures.

4. Conclusions

In summary, we developed a melting method to obtain single-phase $Ag_{1-x}Cu_xIn_5S_8$ alloys using metal sulfides of Ag_2S, Cu_2S and In_2S_3 as precursors. Owing to the complex crystal structure, weak chemical bonding of Ag/Cu–S, and rattling-like Ag/Cu atoms, low κ_{lat} of ~0.63–0.72 Wm^{-1}K^{-1} at 873 K can be obtained in the $Ag_{1-x}Cu_xIn_5S_8$ alloys. By optimizing the κ_{lat} and PF, the peak ZT can reach ~0.31 at 873 K for the n-type $Ag_{0.5}Cu_{0.5}In_5S_8$, which is a bit higher than the theoretical prediction. Due to the strong In–S chemical bonding, $AgIn_5S_8$ has good mechanical properties with a hardness of ~3.95 GPa. We confirmed the mechanism of "rattling-like" phonon modes in $AgIn_5S_8$ by the results of phonon dispersion, Raman spectrum and heat capacity, which can also guide the design of other low-κ_{lat} TE materials. We also systemically studied the defect chemistry of $AgIn_5S_8$ by DFT calculations and experimental trials, providing a guide to further realize the more-promising p-type $AgIn_5S_8$-based alloys and other cubic-spinel TE materials.

Credit author statement

C. Zhang: Data Curation, Software, Writing, Investigation, Methodology, Conceptualization; **Y. Dou and J. Chen:** Data

Curation, Investigation; **S. Fang and W. Xu:** Methodology, Investigation; **X. Wu:** Writing, Methodology, Validation; **L. Hu, F. Liu and Y. Li:** Methodology, Resources; **J. Li:** Conceptualization, Supervision, Writing.

Data availability

The raw/processed data required to reproduce these findings can be reached from the corresponding author through e-mail.

Declaration of competing interest

The authors declare that they have no known competing financial interests or personal relationships that could have appeared to influence the work reported in this paper.

Acknowledgments

This work is supported by the National Natural Science Foundation of China (grant number: 21805196, 52071218), Shenzhen Science and Technology Innovation Commission (grant number: 20200731215211001, 20200814110413001, JCYJ20190808112401659), and Shenzhen Clean Energy Research Institute and the Natural Science Foundation of Shenzhen University.

Appendix A. Supplementary data

Supplementary data to this article can be found online at https://doi.org/10.1016/j.mtener.2022.101029.

References

[1] L.E. Bell, Cooling, heating, generating power, and recovering waste heat with thermoelectric systems, Science 321 (2008) 1457–1461, https://doi.org/10.1126/science.1158899.

[2] G.J. Snyder, E.S. Toberer, Complex thermoelectric materials, Nat. Mater. 7 (2008) 105–114. https://www.nature.com/articles/nmat2090.

[3] J. He, T.M. Tritt, Advances in thermoelectric materials research: looking back and moving forward, Science 357 (2017), eaak9997, https://doi.org/10.1126/science.aak9997.

[4] T. Zhu, Y. Liu, C. Fu, J.P. Heremans, J.G. Snyder, X. Zhao, Compromise and synergy in high-efficiency thermoelectric materials, Adv. Mater. 29 (2017) 1605884, https://doi.org/10.1002/adma.201605884.

[5] Y. Pei, H. Wang, G.J. Snyder, Band engineering of thermoelectric materials, Adv. Mater. 24 (2012) 6125–6135, https://doi.org/10.1002/adma.201202919.

[6] Y. Feng, J. Li, Y. Li, T. Ding, C. Zhang, L. Hu, F. Liu, W. Ao, C. Zhang, Band convergence and carrier-density fine-tuning as the electronic origin of high-average thermoelectric performance in Pb-doped GeTe-based alloys, J. Mater. Chem. 8 (2020) 11370–11380, https://doi.org/10.1039/D0TA02758H.

[7] Y. Tang, Z.M. Gibbs, L.A. Agapito, G. Li, H.S. Kim, M.B. Nardelli, S. Curtarolo, G.J. Snyder, Convergence of multi-valley bands as the electronic origin of high thermoelectric performance in $CoSb_3$ skutterudites, Nat. Mater. 14 (2015) 1223–1228, https://doi.org/10.1038/nmat4430.

[8] P. Li, T. Ding, J. Li, C. Zhang, Y. Dou, Y. Li, L. Hu, F. Liu, C. Zhang, Positive effect of Ge vacancies on facilitating band convergence and suppressing bipolar transport in GeTe-based alloys for high thermoelectric performance, Adv. Funct. Mater. 30 (2020) 1910059, https://doi.org/10.1002/adfm.201910059.

[9] J.P. Heremans, B. Wiendlocha, A.M. Chamoire, Resonant levels in bulk thermoelectric semiconductors, Energy Environ. Sci. 5 (2012) 5510–5530, https://doi.org/10.1039/c1ee02612g.

[10] J. He, S.N. Girard, M.G. Kanatzidis, V.P. Dravid, Microstructure-lattice thermal conductivity correlation in nanostructured $PbTe_{0.7}S_{0.3}$ thermoelectric materials, Adv. Funct. Mater. 20 (2010) 764–772, https://doi.org/10.1002/adfm.200901905.

[11] X. Shen, Y. Xia, C.C. Yang, Z. Zhang, S. Li, Y.H. Tung, A. Benton, X. Zhang, X. Lu, G. Wang, J. He, X. Zhou, High thermoelectric performance in sulfide-type argyrodites compound $Ag_8Sn(S_{1-x}Se_x)_6$ enabled by ultralow lattice thermal conductivity and extended cubic phase regime, Adv. Funct. Mater. 30 (2020) 2000526, https://doi.org/10.1002/adfm.202000526.

[12] S. Lin, W. Li, Z. Bu, B. Gao, J. Li, Y. Pei, Thermoelectric properties of Ag_9GaS_6 with ultralow lattice thermal conductivity, Mater. Today Phys. 6 (2018) 60–67, https://doi.org/10.1016/j.mtphys.2018.09.001.

[13] T. Zhu, L. Hu, X. Zhao, J. He, New insights into intrinsic point defects in V_2VI_3 thermoelectric materials, Adv. Sci. 3 (2016) 1600004, https://doi.org/10.1002/advs.201600004.

[14] L. Abdellaoui, Z.W. Chen, Y. Yu, T. Luo, R. Hanus, T. Schwarz, R.B. Villoro, O. Cojocaru-Miredin, G.J. Snyder, D. Raabe, Y.Z. Pei, C. Scheu, S.Y. Zhang, Parallel dislocation networks and cottrell atmospheres reduce thermal conductivity of PbTe thermoelectrics, Adv. Funct. Mater. 31 (2021) 2101214, https://doi.org/10.1002/adfm.202101214.

[15] W.D. Liu, D.Z. Wang, Q. Liu, W. Zhou, Z. Shao, Z.G. Chen, High-performance GeTe-based thermoelectrics: from materials to devices, Adv. Energy Mater. 10 (2020) 2000367, https://doi.org/10.1002/aenm.202000367.

[16] W. Li, J. Wang, Y. Xie, J.L. Gray, J.J. Heremans, H.B. Kang, B. Poudel, S.T. Huxtable, S. Priya, Enhanced thermoelectric performance of Yb-single-filled skutterudite by ultralow thermal conductivity, Chem. Mater. 31 (2019) 862–872, https://doi.org/10.1021/acs.chemmater.8b03994.

[17] X.L. Shi, J. Zou, Z.G. Chen, Advanced thermoelectric design: from materials and structures to devices, Chem. Rev. 120 (2020) 7399–7515, https://doi.org/10.1021/acs.chemrev.0c00026.

[18] T. Tanimoto, K. Suekuni, T. Tanishita, H. Usui, T. Tadano, T. Kamei, H. Saito, H. Nishiate, C.H. Lee, K. Kuroki, M. Ohtaki, Enargite Cu_3PS_4: a Cu–S-based thermoelectric material with a wurtzite-derivative structure, Adv. Funct. Mater. 30 (2020) 2000973, https://doi.org/10.1002/adfm.202000973.

[19] S. Lin, W. Li, S. Li, X. Zhang, Z. Chen, Y. Xu, Y. Chen, Y. Pei, High thermoelectric performance of Ag_9GaSe_6 enabled by low cutoff frequency of acoustic phonons, Joule 1 (2017) 816–830, https://doi.org/10.1016/j.joule.2017.09.006.

[20] P.J. Ying, X. Li, Y.C. Wang, J. Yang, C.G. Fu, W.Q. Zhang, X.B. Zhao, T.J. Zhu, Hierarchical chemical bonds contributing to the intrinsically low thermal conductivity in alpha-MgAgSb thermoelectric materials, Adv. Funct. Mater. 27 (2017) 201604145, https://doi.org/10.1002/adfm.201604145.

[21] G. Mahan, B. Sales, J. Sharp, Thermoelectric materials: new approaches to an old problem, Phys. Today 50 (1997) 42–47, https://doi.org/10.1063/1.881752.

[22] J.M. Li, H.W. Ming, C.J. Song, L. Wang, H.X. Xin, Y.J. Gu, J. Zhang, X.Y. Qin, D. Li, Synergetic modulation of power factor and thermal conductivity for Cu_3SbSe_4-based system, Mater. Today Energy 18 (2020) 100491, https://doi.org/10.1016/j.mtener.2020.100491.

[23] B. Wang, S. Zheng, Y. Chen, Q. Wang, Z. Li, Y. Wu, J. Li, Y. Mu, S. Xu, J. Liang, Realizing ultralow thermal conductivity in Cu_3SbSe_4 via all-scale phonon scattering by co-constructing multiscale heterostructure and IIIB element doping, Mater. Today Energy 19 (2021) 100620, https://doi.org/10.1016/j.mtener.2020.100620.

[24] T. Deng, T. Xing, M.K. Brod, Y. Sheng, P. Qiu, I. Veremchuk, Q. Song, T.R. Wei, J. Yang, G.J. Snyder, Y. Grin, L. Chen, X. Shi, Discovery of high-performance thermoelectric copper chalcogenide using modified diffusion-couple high-throughput synthesis and automated histogram analysis technique, Energy Environ. Sci. 13 (2020) 3041–3053, https://doi.org/10.1039/d0ee02209h.

[25] G.J. Snyder, T. Caillat, J.P. Fleurial, Thermoelectric properties of chalcogenides with the spinel structure, Mater. Res. Innovat. 5 (2016) 67–73, https://doi.org/10.1007/s100190100133.

[26] D. Carta, M.F. Casula, A. Falqui, D. Loche, G. Mountjoy, C. Sangregorio, A. Corrias, A structural and magnetic investigation of the inversion degree in ferrite nanocrystals MFe_2O_4 (M = Mn, Co, Ni), J. Phys. Chem. C 113 (2009) 8606–8615, https://doi.org/10.1021/jp901077c.

[27] I. Ganesh, A review on magnesium aluminate ($MgAl_2O_4$) spinel: synthesis, processing and applications, Int. Mater. Rev. 58 (2013) 63–112, https://doi.org/10.1179/1743280412Y.0000000001.

[28] M. Schwarz, G. Miehe, A. Zerr, E. Kroke, B.T. Poe, H. Fuess, R. Riedel, Spinel-Si_3N_4: multi-anvil press synthesis and structural refinement, Adv. Mater 12 (2000) 883–887, https://doi.org/10.1002/1521-4095(200006)12:12%3C883::AID-ADMA883%3E3.0.CO;2-C.

[29] W.S. Seo, R. Otsuka, H. Okuno, M. Ohta, K. Koumoto, Thermoelectric properties of sintered polycrystalline $ZnIn_2S_4$, J. Mater. Res. 14 (1999) 4176–4181, https://doi.org/10.1557/jmr.1999.0565.

[30] T. Groń, A. Krajewski, J. Kusz, E. Malicka, I. Okońska-Kozłowska, A. Waśkowska, Thermoelectric power of $CdCr_{2-x}Ga_xSe_4$ p-type spinel semiconductors, Phys. Rev. B 71 (2005), 035208, https://doi.org/10.1103/PhysRevB.71.035208.

[31] K. Hashikuni, K. Suekuni, H. Usui, R. Chetty, M. Ohta, K. Kuroki, T. Takabatake, K. Watanabe, M. Ohtaki, Thermoelectric properties and electronic structures of $CuTi_2S_4$ thiospinel and its derivatives: structural design for spinel-related thermoelectric materials, Inorg. Chem. 58 (2019) 1425–1432, https://doi.org/10.1021/acs.inorgchem.8b02955.

[32] H. Yakhou, A. Maachou, H. Riane, M. Sahnoun, Theoretical investigation of electronic and thermoelectric properties of spinel sulfides A_2BS_4 (A=Sc and Y; B= Cd and Zn), Computational Condensed Matter 21 (2019), e00417, https://doi.org/10.1016/j.cocom.2019.e00417.

[33] F. Majid, M.T. Nasir, E. Algrafy, M. Sajjad, N.A. Noor, A. Mahmood, S.M. Ramay, Exploration of magnesium based MgX_2O_4 (X = Rh, Bi) spinels for thermoelectric applications using density functional theory (DFT), J. Mater. Res. Technol. 9 (2020) 6135–6142, https://doi.org/10.1016/j.jmrt.2020.04.016.

[34] Q. Mahmood, M. Rashid, A. Qurat Ul, N.A. Noor, M.G. Bahar Ashiq, S.M. Ramay, A. Mahmood, Opto-electronic and thermoelectric properties of $MgIn_2X_4$ (X = S, Se) spinels via ab-initio calculations, J. Mol. Graph. Model. 88 (2019) 168–173, https://doi.org/10.1016/j.jmgm.2019.01.010.

[35] R. Juneja, A.K. Singh, Rattling-induced ultralow thermal conductivity leading to exceptional thermoelectric performance in $AgIn_5S_8$, ACS Appl. Mater. Interfaces 11 (2019) 33894–33900, https://doi.org/10.1021/acsami.9b10006.
[36] J.L. Cui, Y.Y. Li, Y. Deng, Q.S. Meng, Y.L. Gao, H. Zhou, Y.P. Li, Microstructure modulation responsible for the improvement in thermoelectric property of a wide-gap $AgIn_5Se_8$ semiconductor, Intermetallics 31 (2012) 217–224, https://doi.org/10.1016/j.intermet.2012.07.013.
[37] Y.-L. Pei, C. Zhang, J. Li, J. Sui, Electrical and thermal transport properties of $AgIn_5Te_8$, J. Alloys. Compd 566 (2013) 50–53, https://doi.org/10.1016/j.jallcom.2013.03.037.
[38] H. Ma, C.-L. Yang, M.-S. Wang, X.-G. Ma, Effects of transport direction and carrier concentration on the thermoelectric properties of $AgIn_5Te_8$: a first-principles study, Mater. Res. Bull. 113 (2019) 77–83, https://doi.org/10.1016/j.materresbull.2019.01.017.
[39] G. Kresse, J. Furthmüller, Efficient iterative schemes for ab initio total-energy calculations using a plane-wave basis set, Phys. Rev. B 54 (1996) 11169–11186, https://doi.org/10.1103/PhysRevB.54.11169.
[40] J.P. Perdew, K. Burke, M. Ernzerhof, Generalized gradient approximation made simple, Phys. Rev. Lett. 77 (1996) 3865–3868, https://doi.org/10.1103/PhysRevLett.77.3865.
[41] G. Kresse, D. Joubert, From ultrasoft pseudopotentials to the projector augmented-wave method, Phys. Rev. B 59 (1999) 1758–1775, https://doi.org/10.1103/PhysRevB.59.1758.
[42] H.J. Monkhorst, J.D. Pack, Special points for Brillouin-zone integrations, Phys. Rev. B 13 (1976) 5188–5192, https://doi.org/10.1103/PhysRevB.13.5188.
[43] K. Momma, F. Izumi, VESTA 3 for three-dimensional visualization of crystal, volumetric and morphology data, J. Appl. Crystallogr. 44 (2011) 1272–1276, https://doi.org/10.1107/s0021889811038970.
[44] A. Togo, I. Tanaka, First principles phonon calculations in materials science, Scr. Mater. 108 (2015) 1–5, https://doi.org/10.1016/j.scriptamat.2015.07.021.
[45] A. Savin, R. Nesper, S. Wengert, T.F. Fassler, ELF: the electron localization function, Angew. Chem. Int. Ed. Engl. 36 (1997) 1809–1832, https://doi.org/10.1002/anie.199718081.
[46] N.S. Orlova, I.V. Bodnar, E.A. Kudritskaya, Crystal growth and properties of the $CuIn_5S_8$ and $AgIn_5S_8$ compounds, Cryst. Res. Technol. 33 (1998) 37–42, https://doi.org/10.1002/(sici)1521-4079(1998)33:1<37::Aid-crat37>3.0.Co;2-m.
[47] P. Villars, A. Prince, H. Okamoto, Handbook of Ternary Alloy Phase Diagrams, ASM International, 1995.
[48] G.J. Snyder, A.H. Snyder, M. Wood, R. Gurunathan, B.H. Snyder, C. Niu, Weighted mobility, Adv. Mater. 32 (2020) 2001537, https://doi.org/10.1002/adma.202001537.
[49] H.-S. Kim, Z.M. Gibbs, Y. Tang, H. Wang, G.J. Snyder, Characterization of Lorenz number with Seebeck coefficient measurement, Apl. Mater. 3 (2015), 041506, https://doi.org/10.1063/1.4908244.
[50] S. Wang, J.R. Salvador, J. Yang, P. Wei, B. Duan, J. Yang, High-performance n-type $Yb_xCo_4Sb_{12}$: from partially filled skutterudites towards composite thermoelectrics, NPG Asia Mater. 8 (2016) e285, https://doi.org/10.1038/am.2016.77.
[51] W.G. Zeier, J. Schmitt, G. Hautier, U. Aydemir, Z.M. Gibbs, C. Felser, G.J. Snyder, Engineering half-Heusler thermoelectric materials using Zintl chemistry, Nat. Rev. Mater. 1 (2016) 16032, https://doi.org/10.1038/natrevmats.2016.32.
[52] K. Biswas, J. He, I.D. Blum, C.I. Wu, T.P. Hogan, D.N. Seidman, V.P. Dravid, M.G. Kanatzidis, High-performance bulk thermoelectrics with all-scale hierarchical architectures, Nature 489 (2012) 414–418, https://doi.org/10.1038/nature11439.
[53] J. Li, S. Zhang, F. Jia, S. Zheng, X. Shi, D. Jiang, S. Wang, G. Lu, L. Wu, Z.-G. Chen, Point defect engineering and machinability in n-type Mg_3Sb_2-based materials, Mater. Today Phys. 15 (2020) 100269, https://doi.org/10.1016/j.mtphys.2020.100269.
[54] G. Bai, Y. Yu, X. Wu, J. Li, Y. Xie, L. Hu, F. Liu, M. Wuttig, O. Cojocaru-Mirédin, C. Zhang, Boron strengthened GeTe-based alloys for robust thermoelectric devices with high output power density, Adv. Energy Mater. 11 (2021) 2102012, https://doi.org/10.1002/aenm.202102012.
[55] L.D. Zhao, B.P. Zhang, J.F. Li, M. Zhou, W.S. Liu, J. Liu, Thermoelectric and mechanical properties of nano-SiC-dispersed Bi_2Te_3 fabricated by mechanical alloying and spark plasma sintering, J. Alloys Compd. 455 (2008) 259–264, https://doi.org/10.1016/j.jallcom.2007.01.015.
[56] B. Li, P. Xie, S. Zhang, D. Liu, Lead germanium telluride: a mechanically robust infrared high-index layer, J. Mater. Sci. 46 (2011) 4000–4004, https://doi.org/10.1007/s10853-011-5327-9.
[57] T. Dahal, S. Gahlawat, Q. Jie, K. Dahal, Y. Lan, K. White, Z. Ren, Thermoelectric and mechanical properties on misch metal filled p-type skutterudites $Mm_{0.9}Fe_{4-x}Co_xSb_{12}$, J. Appl. Phys. 117 (2015), 055101, https://doi.org/10.1063/1.4906954.
[58] Z. Liu, W. Gao, X. Meng, X. Li, J. Mao, Y. Wang, J. Shuai, W. Cai, Z. Ren, J. Sui, Mechanical properties of nanostructured thermoelectric materials α-MgAgSb, Scr. Mater. 127 (2017) 72–75, https://doi.org/10.1016/j.scriptamat.2016.08.037.
[59] C. Chang, L.D. Zhao, Anharmoncity and low thermal conductivity in thermoelectrics, Mater. Today Phys. 4 (2018) 50–57, https://doi.org/10.1016/j.mtphys.2018.02.005.
[60] Z. Chen, X. Zhang, Y. Pei, Manipulation of phonon transport in thermoelectrics, Adv. Mater. 30 (2018) 1705617, https://doi.org/10.1002/adma.201705617.
[61] J. Callaway, H.C. von Baeyer, Effect of point imperfections on lattice thermal conductivity, Phys. Rev. 120 (1960) 1149–1154, https://doi.org/10.1103/PhysRev.120.1149.
[62] A. Li, C. Fu, X. Zhao, T. Zhu, High-performance Mg3Sb2-xBix thermoelectrics: progress and perspective, Research 2020 (2020) 1934848, https://doi.org/10.34133/2020/1934848.
[63] C.G.V.d. Walle, J. Neugebauer, First-principles calculations for defects and impurities: applications to III-nitrides, J. Appl. Phys. 95 (2004) 3851–3879, https://doi.org/10.1063/1.1682673.
[64] S.M. Sze, K.K. Ng, Physics of Semiconductor Devices, John Wiley & Sons, New Jersey, 2006.

Chaohua Zhang received his B.S. degree in physics from Lanzhou University in 2008, and received a Ph.D. degree in physical chemistry under the supervision of Prof. Zhongfan Liu from Peking University in 2013. After three years post-doctoral experience in Prof. Qihua Xiong's group at Nanyang Technological University, he joined Shenzhen University as an associate professor in 2017. His current research is focused on the control growth of 2D materials, synthesis and characterization of thermoelectric materials.

Xuelian Wu received her ME and Ph.D. degree in Chemical Engineering from Sichuan University and the University of New South Wales (UNSW) in 2014 and 2018, respectively. After that she worked as a postdoctoral research associate at Shenzhen University. She is now a research associate at College of Materials Science and Engineering, Shenzhen University. Her current research interests primarily focus on the design and fabrication of two-dimensional Bi-based materials for energy-related applications.

Junqin Li is a Professor in the College of Materials and Engineering, Shenzhen University since 2001. He received his PhD in materials physics and chemistry from City University of Hong Kong in 1999. He worked as a post-doctoral research fellow in Brunel University from 1999 to 2001. His research interests are focused on the phase relationship, crystal structures, microstructures and physical properties of high-performance energy storage and conventional materials, such as batteries, magneto-caloric and thermoelectric materials.